Chapter 3

Modelling the energy balance at the snow surface

This chapter presents a review of background theory to compute the components of the energy balance at the snow surface. Most of the time analytical solutions to the problems described in the theory are rather difficult to implement. In this cases the modelling tools and empirical or semi-empirical approaches, will be described and the reason for choosing any particular approach highlighted. The models will be tested against data collected not only in the Andes, but also in the Alps, which may add reliability to the wider application of the selected tool.

The incorporation of topography into the energy balance will be addressed in chapters 4 and 6. The effect of albedo variability will be addressed in Chapter 5 and the energy balance at a microtopographical scale, that of the surface ablation forms, in Chapter 6.

3.1 Introduction

The net energy flux Q at the surface of the glacier can be expressed as:

$$Q = I_G(1 - \alpha) + L\downarrow - L\uparrow + H + L_v E + Q_s \tag{3.1}$$

where I_G is global short–wave radiation, α is snow albedo, L is long–wave radiation, arrows indicating downward or upward fluxes, H and $L_e E$ are sensible and latent turbulent fluxes with the atmosphere and Q_s is internal heat flux within the snow pack. Following the general convention, fluxes toward the surface are positive.
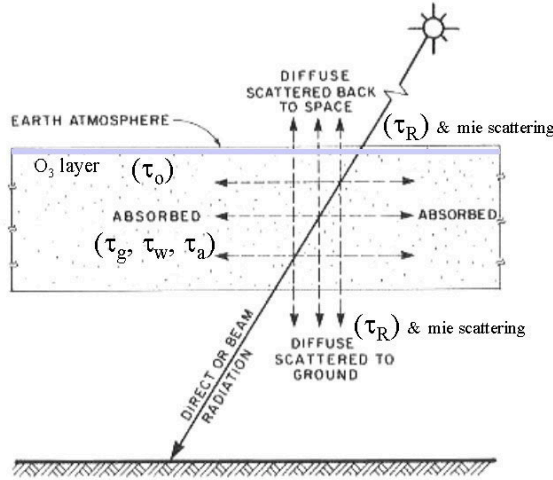
Figure 3.1. schematic representation of the effect of the earth's atmosphere on the short–wave radiation from the sun. The attenuation, absorption transmittance and scattering, either forward to ground, back to space and multiple scattering are formidable problems to solve for a real atmosphere. An empirical solution with satisfactory results will be presented in the following sections. Adapted from Iqbal (1983).

3.2 Short–wave radiation

As we have seen in Chapter 2, the input of solar radiation during the ablation season in the Central Andes is one of the highest in the world. Short–wave solar fluxes are the main energy input for ablation, as in many mountain glaciers (e.g. Wagnon et al. 1999), and given the lack of observations and permanent meteorological stations in this geographical area, it would be desirable to find a model of solar radiation that can be applied with confidence to a glacierised basin in the region. The advantage here is that the ablation season is generally stable, with clean and clear atmospheres, which make the modelling task easier.

3.2.1 Background theory

To estimate the solar radiation falling on the glacier surface, we need to calculate the absorption, reflection and transmission through the atmospheric path between the snow surface and the top the atmosphere; it is equivalent to solving the radiative transfer equation through that path (Figure 3.1).

Let us consider first the case where only absorption occurs. It is generally assumed that absorptance of a monochromatic beam (N_λ) through an infinitesimal distance ds is independent of N_λ but proportional to the density of the transmitter $\rho(s)$, which will be denoted simply by ρ from now on, and to ds (Paltridge and Platt 1976), thus:

$$dN_\lambda/N_\lambda = -\kappa_{a\lambda}\rho\, ds \tag{3.2}$$

where $\kappa_{a\lambda}$ is defined as the spectral absorption coefficient of the medium. Integrating along a finite path

from x_1 to x_2 gives:

$$N_\lambda = N_{\lambda 0} e^{-\kappa_{a\lambda} \int_{x_1}^{x_2} \rho\,ds} \tag{3.3}$$

which is formally known as Beer's Law. When the spectral absorption coefficient is a function of position it should be written inside the integral. The quantity $\int_{x_1}^{x_2} \rho(s)ds$ (dimensions $kg\,m^{-2}$) is defined as the optical path and the dimensionless quantity $-\kappa_{a\lambda} \int_{x_1}^{x_2} \rho(s)ds$ is called the optical depth (Paltridge and Platt 1976). When considering the atmosphere in reference to the direct solar beam, the optical path is called the absolute optical air mass:

$$m_a = \int_0^\infty \rho\,ds \tag{3.4}$$

For the vertical direction, ds is substituted by dz, the increment in vertical height. For an oblique trajectory of the solar beam the relative optical air mass is defined as the ratio of the optical path along the oblique trajectory to the vertical path in the zenith direction:

$$m_a = \int_0^\infty \rho\,ds \left/ \int_0^\infty \rho\,dz \right. \tag{3.5}$$

A similar situation can be described for a pure scattering medium:

$$N_\lambda = N_{\lambda 0} e^{-\int_{x_1}^{x_2} \beta_{sc} \rho\,ds} \tag{3.6}$$

where β_{sc} is the volume scattering coefficient (dimensions m^{-1}).

A beam traversing a medium in a given direction is subjected to both attenuation and augmentation processes. Augmentation may happen due to forward scattering and by radiative emission of the medium. In the latter case, the main radiative contribution along the atmospheric path is likely to be in the thermal radiation band, which will be considered in Section 3.3.

The scattering process becomes more complicated when we consider the actual composition of the atmosphere and atmospheric particles. In theory, the scattering of radiation by spherical particles can be derived from the solution of Maxwell's electromagnetic equations in spherical polar coordinates. One of those solutions is given by Rayleigh's theory, which applies to air molecules of size smaller than one tenth of the wavelength of light. The mathematical treatment of light scattering can be classified according to the parameter $2\pi r/\lambda$ and the index of refraction n, where r is the radius of the particle and λ the wavelength in micrometres. We have then three cases (Iqbal 1983):
- $2\pi r/\lambda < 0.6/n$, scattered is described by Rayleigh's theory;
- $2\pi r/\lambda > 5$ uncommon in the earth's atmosphere;
- $0.6/n < 2\pi r/\lambda < 5$ scattering described by Mie's Theory.

For simplicity, Iqbal's (1983) expression has been reproduced, but it should be noted that the refraction index is a complex number. Mie theory gives a solution for the scatter produced by an isolated sphere, and it is in principle possible to treat also irregular particles by considering that due to their

random orientation their average behaviour can be represented as a sphere of equivalent size (Paltridge and Platt 1976). This is not true for preferentially aligned particles, like ice crystals in cirrus clouds, although it can be acceptable for cloudless atmospheres.

The analytical solution of the radiative transfer equation including absorption and scattering can be formidable, and therefore different numerical solutions and simplifications have been developed. Two of these are the two-stream and Eddington approximations. For an overview the reader is directed to the work of Paltridge and Platt (1976, chapter 4) and Jacobson (1999, Section 10.8.3), where extensive references are supplied.

We have been dealing, up to now, with monochromatic radiation, a single wavelength, but for the practical purpose of estimating the energy balance at the snow surface we are more interested in the total energy supplied by the short–wave broadband radiation flux as a whole. The spectral distribution, however, is useful for deriving snow properties and for the remote sensing of the snow cover. There are models that, by applying semi-analytical and numerical solutions to the radiative transfer problem, successfully calculate the transmittances for any given wavelength band (Berk et al. 1989, Vermote et al. 1994, Vermote et al. 1997). The accuracy of these models, based on a line–by–line calculation and extensive databases of atmospheric components, is remarkable (Figure 3.2), however their application is rather time consuming and computer demanding. In order to model the solar radiation over a large time span, its daily or hourly variation and to incorporate the effect of topography, we need a simpler, yet accurate model. This is also needed in other fields of research, such as plant ecology, solar engineering and architecture or the implementation of general circulation models. Therefore considerable effort has been made successfully in that direction. A review of different parametric models to estimate solar short–wave radiation is given by Niemelä et al. (2001b), and the model that, despite its simplicity, gives better results in that intercomparison is Iqbal's (1983) model. This latter model is actually a slight modification of Bird and Hulstrom model (Bird and Hulstrom 1981a, Bird and Hulstrom 1981b), that somehow has passed to history as Iqbal's model.

3.2.2 Bird and Hulstrom (Iqbal) parametric model

Bird and Hulstrom compare the outputs of seven simple models with that of the rigorous model SOLTRAN, based on the atmospheric transmission model LOWTRAN. In this latter model the band absorption model is based on laboratory measurements and theoretical molecular line constants in line–by–line calculations (Bird and Hulstrom 1981a); absorption coefficients from different absorbers are stored at a 5 cm^{-1} wavenumber (the inverse of wavelength) intervals and the transmittance is calculated with a resolution of 20 cm^{-1} interval. The scattering and absorption by aerosols is computed according to MIE theory and is stored in the code as a function of wavelength. For the atmospheric profile the model allows the input of radiosonde data or the use of four standard aerosol models. For a more recent version of this model, which is continually updated, see Berk et al. (1989).
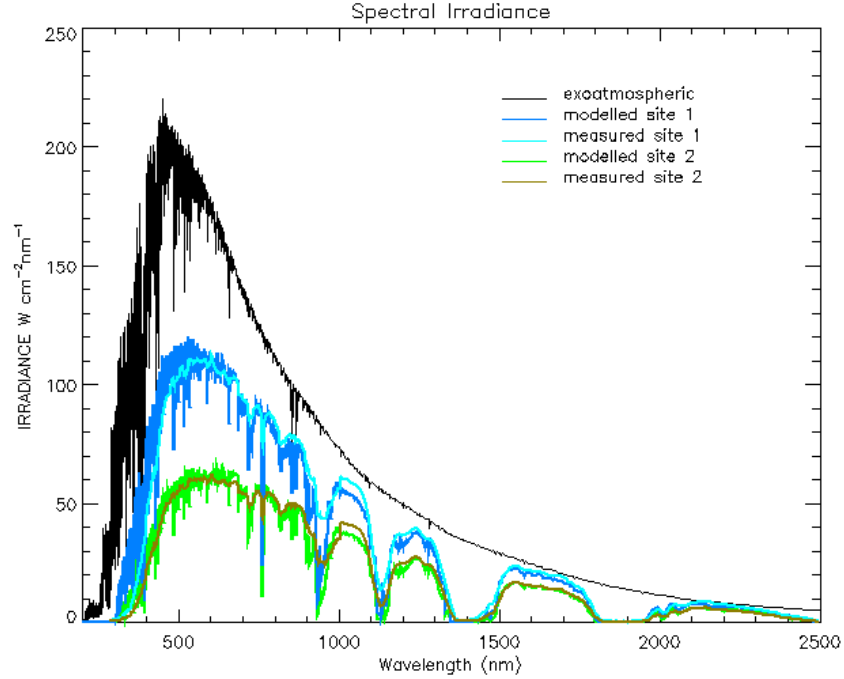
Figure 3.2. Comparison between modelled and measured radiation spectral distribution outside the atmosphere and on the ground for two sites near Edinburgh, 55.92°N, 3.17°W, in summer. The modelled values are the output of the radiative transfer model MODTRAN using estimated visibility and incorporated model atmospheres, measurements were performed by the author with a GER 3700 spectroradiometer.

Direct radiation

The expressions from the seven simple models compared by Bird and Hulstrom were tuned to get the best least squares fit to the output of the SOLTRAN model. The expression of direct normal irradiance was further modified in the present work to:

$$I_n = 0.9751 \, I_0 \left(\tau_r \tau_o \tau_g \tau_w \tau_a + \beta(z) \right) \tag{3.7}$$

where the factor 0.9751 is the ratio of the extraterrestrial irradiance in the spectral interval considered by the SOLTRAN model (0.3 μm to 3.0 μm) to the solar constant I_{sc}; $I_0 = I_{sc}(R_0/R)^2$ is the extraterrestrial solar radiation or solar constant corrected for the eccentricity of the earth's orbit by multiplying it by the reciprocal of the square of the radius vector of the earth, calculated following Spencer (1971), as shown in Equation 5.19; the τ functions are transmittance functions for Rayleigh scattering and transmittance due to ozone, uniformly mixed gases, water vapour and aerosols respectively; and β_z is a correction term for altitude explained below.

This expression differs slightly from Bird and Hulstrom's formulation in two ways. Firstly the

factor 0.9751 was originally 0.9662 as the original computation followed Thekaekara's (1973) value of 1353 Wm^{-2} for the solar constant. Iqbal corrected the value for the more updated NASA/ASTM solar constant of 1367 Wm^{-2} and its spectral distribution. The present–day accepted value of the solar constant is 1366.1 Wm^{-2} computed as the mean of daily averages from six different satellites over the 1978-1998 time period. (Fröhlich and Lean 1998). The second difference is the correction for increased transmittance with altitude: $\beta(z)$ (units: m^{-1}). This term is introduced following Bintanja (1996) who applied it to the parameterisation of radiative fluxes in Antarctica:

$$
\begin{aligned}
\beta(z) &= 2.2 \times 10^{-5}\, z & \text{for } z \leqslant 3000m \\
\beta(z) &= 2.2 \times 3000 \times 10^{-5} & \text{for } z > 3000m
\end{aligned}
\tag{3.8}
$$

where z is the altitude above sea level. $\beta(z)$ is strongly linear up to 3000 m and fairly constant up to 5-6000 m.

Note that the spectral interval is from 0.3 μm to 3.0 μm and this ignores some of the incoming solar radiation, actually about 14 Wm^{-2} in the ultraviolet and 24 Wm^{-2} in the near infrared, in total about 2.8% of the total extraterrestrial radiant flux according to data from the World Radiation Centre (WRC) in Davos, Switzerland (Iqbal 1983, pp. 46-47). The ultraviolet band is entirely absorbed by the ozone layer before reaching the altitudes in which we are working. In relation to the near infrared region of the spectrum it is interesting to notice, as remarked by Paltridge and Platt (1976), that outside the atmosphere only 0.4% of the radiant energy is in wavelengths longer than 5 μm, whereas in the infrared band, only 0.4% of the energy is within wavelengths shorter than 5 μm, and the transition after atmospheric absorption is at a point closer to 2 μm. Therefore the solar and terrestrial radiation bands can be treated independently and the sensitivity range of the pyranometers used here seem appropriate for the solar radiation treatment.

Firstly, we calculate the relative optical air mass (m_r) according to Iqbal (1983), which gives a formula that approximate values of a model atmosphere as:

$$
m_r = 1.0/(\cos\theta + 0.15(93.885 - \theta_d)^{-1.253})
\tag{3.9}
$$

where θ_d is $\theta\,(180/2\pi)$ or zenith angle in degrees.

The solution of Equation 3.5, the formal definition of airmass, can only be obtained if the vertical density variation of the actual atmosphere is known. This approximation is for standard pressure, a further approximation for local conditions at pressure p_z is given by the relative optical air mass pressure corrected (m_a):

$$
m_a = m_r \frac{p_z}{1013.25}
\tag{3.10}
$$

Pressure as a function of altitude was calculated following the equation derived for the US standard

atmosphere 1976 (U.S. NOAA 1976, p. 12 & 13):

$$p_z = \left(\frac{p_0 T_0}{T_0 + L_M(H - H_b)} \right)^{\frac{g_0' M_d}{R^* L_M}} \tag{3.11}$$

where H is geopotential altitude as defined in Equation 3.12, H_b is reference pressure level, which is 0 m for the first 11 km in the atmosphere and L_M is the molecular scale temperature gradient in K/km′ (-6.5 °K), where m′ is the standard geopotential metre. g_0' is a dimensional constant to relate the standard geopotential meter to geometric height. It is numerically equal to g_0, the sea level value of the acceleration of gravity (= 9.80665 m/s^2), which applies precisely to a latitude of 45 ° 32′ 33″. M_d is the molecular weight of dry air (= 0.028966 $kg\,mol^{-1}$) and R^* is the universal gas constant (= 8.31432 $Jmol^{-1}K^{-1}$). The geopotential altitude is calculated as:

$$H = \frac{r_0 z}{r_0 + z} \tag{3.12}$$

where r_0 is the effective earth's radius at a specific latitude (= 6.356766×10^6 m for the US standard atmosphere). The value of r_0 takes into account the centrifugal acceleration at the particular latitude to be consistent with the sea-level value of the acceleration of gravity. z is altitude above sea level.

The calculation of the individual transmittances follows Bird and Hulstrom (1981b). Transmittance by ozone:

$$\tau_o = 1.0 - [0.1611\,lm_r(1.0 + 139.48\,lm_r)^{-0.035}$$
$$-0.002715\,lm_r(1.0 + 0.044\,lm_r + 0.0003(lm_r)^2)^{-1}] \tag{3.13}$$

$$\tag{3.14}$$

where l is the vertical ozone layer thickness in cm, which is updated according to data from the Total Ozone Mapping Spectrometer–Earth Probe (TOMS–EP 2001).

Transmittance by uniformly mixed gases:

$$\tau_g = e^{-0.0127\,m_a^{0.26}} \tag{3.15}$$

Transmittance by water vapour:

$$\tau_w = 1.0 - 2.4959wm_r[(1.0 + 79.034wm_r^{0.6828} + 6.385wm_r]^{-1} \tag{3.16}$$

where w is precipitable water in cm calculated after Prata (1996) as in Equation 3.28

The transmittance by aerosols is a complicated task when there is no direct information on atmospheric turbidity. Thus some surrogate variable, easily measurable in the field, needs to be used. For

the implementation of the present model, Iqbal's formulation relies on visibility, which is derived from Mächler's (1983) work. Visibility is calculated as the maximum distance at which the naked eye can distinguish objects. This is a rather subjective value, especially when considering that aerosol transmittance is probably the most important parameter affecting atmospheric extinction of short–wave radiation (Bird and Hulstrom 1981b). However, the advantage of the study site is that skies are normally very transparent, with visibility ranges in excess of 100 km. Transmittance by aerosols is computed as:

$$\tau_a = \left[0.97 - 1.265\,(Vis)^{-0.66}\right] m_a^{0.9} \tag{3.17}$$

where Vis is visibility in km.

Diffuse radiation from the sky

For the diffuse component of solar radiation, Bird and Hulstrom (1981a) give the following parametric equations:

The Rayleigh-scattered diffuse irradiance after the first pass through the atmosphere is given by:

$$I_{dr} = 0.79\,I_0 \cos\theta\,\tau_o\tau_g\tau_w\tau_{aa}\,0.5\,(1.0 - \tau_r)/(1.0 - m_a + m_a^{1.02}) \tag{3.18}$$

where τ_{aa} is the transmittance of direct radiation due to aerosol absorptance:

$$\tau_{aa} = 1.0 - (1.0 - \omega_0)(1.0 - m_a + m_a^{1.06})(1.0 - \tau_a) \tag{3.19}$$

ω_0 is the single scattering albedo, the fraction of the incident energy scattered to total attenuation by aerosols, taken as 0.9 (Hoyt 1978, Bird and Hulstrom 1981b, Iqbal 1983).

The aerosol-scattered diffuse irradiance after the first pass through the atmosphere is:

$$I_{da} = 0.79\,I_0 \cos\theta\,\tau_o\tau_g\tau_w\tau_{aa}\,F_c\,(1.0 - \tau_{as})/(1.0 - m_a + m_a^{1.02}) \tag{3.20}$$

where $\tau_{as} = \tau_a/\tau_{aa}$ and F_c is the fraction of forward scattering to total scattering. If no information on aerosols is available, Iqbal's model recommends a value of 0.84.

To compute the multiply-reflected irradiance, the atmospheric albedo is computed as:

$$\alpha_a' = 0.0685 + (1.0 - F_c)(1.0 - \tau_{as}) \tag{3.21}$$

The diffuse irradiance from multiple reflections between the earth and the atmosphere is calculated as:

$$I_{dm} = (I_n \cos\theta + I_{dr} + I_{da})\,\alpha_g\,\alpha_a'\,/(1.0 - \alpha_g\alpha_a'), \tag{3.22}$$
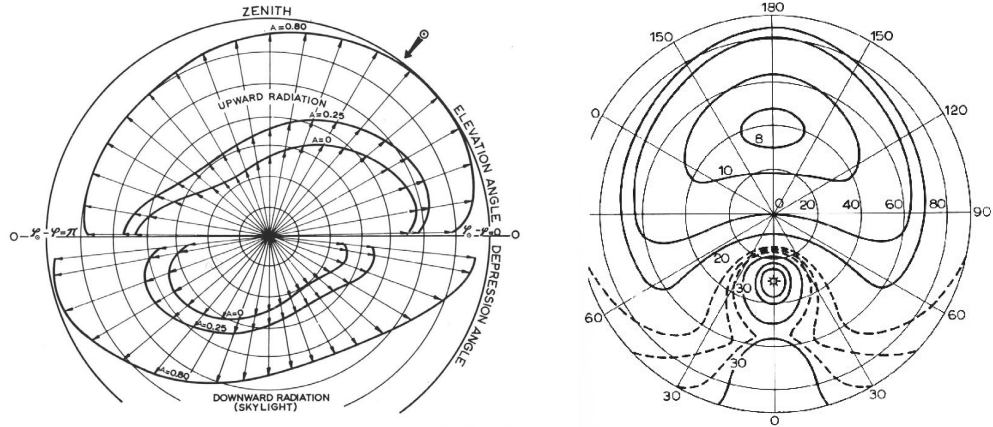
Figure 3.3. Distribution of skylight and upward radiation for three different surface albedos A, from Coulson (1959) as cited by Paltridge and Platt (1976, p. 114). The sun's elevation is 53°, its position is given by the symbol ← ⊙. Right figure is sky luminance distribution as quoted by Robison (1966), cited by Paltridge and Platt (1976, p. 115)

where α_g is the albedo of the ground. The value of α_g is estimated from local knowledge of the average snow cover in a few km around the site of interest, as explained by Greuell et al. (1997) and shown in Chapter 5, Equation 5.25.

Finally, total diffuse radiation is:

$$I_d = I_{dr} + I_{da} + I_{dm} \tag{3.23}$$

The diffuse component of solar radiation in the atmosphere is considered as having an isotropic distribution. This is far from reality, as can be seen even by the naked eye when comparing the sky luminosity near the horizon with the circumsolar region, or the area at 90 ° to the sun. This is further confirmed by a simple experiment, such as comparing the readings of the light meter of a reflex camera on the aforementioned regions of the sky. The volume distribution of incoming and outgoing diffuse radiation has been investigated for a long time (e.g. Kondratiev 1969) and results for model atmospheres are exemplified in Figures 3.3, taken from Coulson (1959). However, as the objective in this work is to calculate total energy falling on a inclined surface surrounded by rough topography, it is intuitive that the integration of the anisotropic diffuse radiation field over a whole day will be approximately equivalent to an isotropic field. Furthermore, at high altitude the diffuse component is much reduced, and therefore the errors derived from an isotropic approach are smaller.

3.2.3 Diffuse reflected radiation

In mountainous terrain, especially when covered in snow, an important component of the total diffuse radiation is due to the reflection of light on the surrounding slopes. Ignoring this component may lead to gross errors in the estimation of the energy balance terms (Klok and Oerlemans 2002).

The effect of topography is twofold; firstly, it reduces part of the diffuse radiation coming from the sky by sheltering a fraction of the sky near the horizon, and secondly, it enhances diffuse radiation by reflecting global radiation onto the surrounding slopes. Both effects are opposed but do not cancel each other out and the diffuse reflected component can be very important when the surrounding slopes have a high albedo. Thus, the global incoming flux density I_G at any given zenith angle θ will be:

$$I_G = I_{dir} \cos \theta + \int I_{dif} \, d\omega \tag{3.24}$$

where the first term is direct solar beam and the second is diffuse radiation integrated over all solid angles (ω) of the upper hemisphere (Paltridge and Platt 1976). This is a formidable computational task even for idealised relief (Peterson et al. 1985). The task is even more complex for an area of irregular topography, and a simplification is necessary. The problem is tackled by introducing the concept of skyview factor (Section 4.6), and the approach is explained in Section 5.3.2, Equations 5.22 onwards.

Despite the necessary simplifications this model performs very well in clean atmospheres like those at high altitude in the Andes, as can be seen from figure 3.5, which compares modelled and measured data at 4667 m a.s.l. The modelled data include direct, diffuse and diffuse reflected radiation, but do not include cast shadows, which will be incorporated later in Section 4.5.

3.3 Long–Wave radiation

The downwelling long–wave radiative flux at the surface of the glacier for clear skies depends on the temperature, constitution and vertical profile of the overlying atmosphere, plus the emitted radiation from surrounding slopes. A good approximation to the atmospheric component is:

$$L \downarrow = - \int_0^\infty \int_{p_s}^0 \pi B_\gamma \left[T(p) \right] \frac{dt_\gamma(p_s, p)}{dp} dp \, d_\gamma \tag{3.25}$$

where p is pressure, p_s is surface pressure, T is temperature, γ is wavelength, B_γ is the monochromatic Planck function and $t_\gamma(ps, p)$ is the monochromatic flux transmissivity from p to p_s (Niemelä et al. 2001a). A rigorous solution to this equation requires a detailed knowledge of the vertical variation in T, p and $t_\gamma(ps, p)$, which was not available for the present case studies. Thus, an approximate solution based on meteorological variables recorded at screen level is desirable.

Niemelä et al. (2001a) has done a comprehensive evaluation of several parameterisations and compared them to *measured* values in Finland over a temperature range of -49° C to +11° C. The italics are to stress that the actual downward long–wave flux was estimated from measured net total flux, measured net short–wave and estimated surface temperature. The possible errors in this estimation are given in Niemelä et al. (2001a, Equation 16 onwards). From this intercomparison, the best results were obtained from parameterisations used in the numerical weather prediction models (NWP), which require vertical atmospheric profile inputs. The following best results were the formulae proposed by Prata (1996) and Dilley and O'Brien (1998). Dilley and O'Brien's (1998) model performs better in wet environments, while Prata's (1996) approach is better suited to dry atmospheres (Dilley and O'Brien 1998, Niemelä et al. 2001a). It also includes a correction for non sea level pressures different, which makes it more appropriate for use in mountain environments.

The approach of both authors is to calculate the emissivity term ϵ_a considering the whole atmosphere as a *grey* body radiator:

$$\epsilon_a = \frac{L\downarrow}{\sigma T^4} \tag{3.26}$$

where σ is the Stephan-Boltzmann's constant. Prata (1996) and Niemelä et al. (2001a) review different equations, which are based in empirical observations, with some methods having their basis in the radiative transfer theory (Niemelä et al. 2001a). These parameterisations calculated emissivity either as a function of water vapor pressure e_0, screen temperature T, or both. As a result Prata proposed a new formulation, based on precipitable water, *i.e.* indirectly on both e_0 and T:

$$\epsilon_a = 1 - (1 + w_p)\,e^{-(1.2 + 3w_p)^{0.5}} \tag{3.27}$$

where precipitable water (w_p) is calculated following an empirical equation given also by Prata (1996):

$$w_p = 46.5\frac{e_0}{T_a} \tag{3.28}$$

where T_a is screen level air temperature in K. The actual vapour pressure is $e_0 = e^* RH$, where e^* is saturated vapour pressure computed following Lowe's (1977) polynomials (Equation 3.30), and RH is relative humidity from 0.0 to 1.0. This equation best fits extensive data from radiosonde stations around the world, and it is for standard pressure, which certainly is not the case in the Andes. The column of water above the site of interest is much smaller at 4600 m than at sea level, and therefore this correction needs to be taken into acount. Prata gives a precise derivation of the relationship between vapor pressure and precipitable water, which requires knowledge of the scale height of the atmosphere and the lapse rate, and the solution is a degenerate hypergeometric function (for a general description of this type of function see for example Weisstein (1999), and for a detailed discussion see Gradshteyn and Ryzhik (1980)). For simplicity, speed of implementation and because of the lack of information about the atmospheric conditions aloft, an empirical formula suggested by Paltridge and Platt (1976) is used

here. Thus, the correction of precipitable water to the datum conditions is:

$$w_p = w' \left(\frac{p_z}{103.25}\right)^{3/4} \left(\frac{273}{T_a}\right)^{1/2} \tag{3.29}$$

here w' is the result of Equation 3.28 and p_z is local pressure at height z.

Lowe's (1977) polynomials for the calculation of saturation vapour pressure are as follows:

Over water:

$$
\begin{aligned}
a_0 &= 6984.505294 \\
a_1 &= -188.9039310 \\
a_2 &= 2.133357675 \\
a_3 &= -1.288580973e-2 \\
a_4 &= 4.393587233e-5 \\
a_5 &= -8.023923082e-8 \\
a_6 &= 6.136820929e-11
\end{aligned}
$$

$$e^* = a_0 + T(a_1 + T(a_2 + T(a_3 + T(a_4 + T(a_5 + Ta_6))))) \tag{3.30}$$

For the saturation vapour pressure over ice, the polynomials are:

$$
\begin{aligned}
T &= T - 273.15 \\
a_0 &= 6.109177956 \\
a_1 &= 5.03469897e-1 \\
a_2 &= 1.886013408e-2 \\
a_3 &= 4.176223716e-4 \\
a_4 &= 5.824720280e-6 \\
a_5 &= 4.838803174e-8 \\
a_6 &= 1.838826904e-10
\end{aligned}
$$

and then also are applied to Equation 3.30

Finally the effect of sky obstruction and long–wave emission by surrounding slopes is considered in a similar way as for short–wave radiation, using the sky view factor. This approach has been widely used before (Olyphant 1986b, Duguay 1995, Plüss and Ohmura 1997). Incoming Long–wave radiation is:

$$L \downarrow = \epsilon_a \sigma T^4 f_v + \epsilon_s \sigma T^4 (1 - f_v) \tag{3.31}$$

where, ϵ_s is snow emissivity, taken as 0.99, σ is the Stephan-Boltzman constant and the sky view factor f_v is defined in Section 4.6.

Different parameterisations have been proposed to evaluate the effect of cloudiness on downward long–wave radiation (Brutsaert 1982, pp. 142–144; for a review see Oke 1987). These parameterisations require information on the type of clouds, fraction of sky covered by all or every type, and ideally the base height and temperature of the cloud. This information is not available for the present study.

3.4   Turbulent heat transfer

Interchange of energy between the snow surface and the lower part of the atmospheric boundary layer (surface sublayer) takes place mainly in the form of vertical transfer by convective motion. By comparison, molecular diffusivity is insignificant, and about five orders of magnitude smaller (Paterson 1994). In the present study we are interested in the transfer of two entities: heat and water vapour. Transfer of water vapour means evaporation or condensation, and the related absorption or liberation of latent heat. The associated energy flux is computed by multiplying the mass interchange of water vapour by the latent heat of sublimation when the snow is dry or by the latent heat of evaporation when there is water present (Greuell and Konzelmann 1994). The best approach to evaluate convective fluxes is by the eddy fluctuation or eddy correlation method (Oke 1987, Munro 1989). This method requires delicate instruments that can detect instantaneous variation in the vertical velocity of wind and of any entity under study (e.g. water vapour), and recording equipment capable of processing large amounts of information. It is clear that these requirements render the method inappropriate for a light expedition to high altitude glaciers, and therefore an alternative method is necessary. A second approach is using an aerodynamic profile, which requires the measurement of wind, temperature and humidity at various levels above the surface. This approach necessitates a moderate amount of instrumentation but is very sensitive to instrumental error, and as Denby and Greuell (2000) have shown its theoretical application is highly questionable over a glacier in the presence of katabatic winds.

The method employed in this study was the bulk-transfer method, as explained by Munro (1989), using the Monin–Obukhov stability length with the formulation presented by Brutsaert (1982), and the scalar roughness lengths corrections suggested by Andreas (1986). The approach has been used successfully in areas of similar climatic conditions, where evaporation is likely to be important (Marks and Dozier 1992, Aizen et al. 1997). In this approach temperature, wind speed and humidity are measured at one single level, usually at 2 m above the surface. Humidity at the snow surface is considered to be at the saturation point for the corresponding temperature of the snow, which is zero for melting conditions and very problematic to determine for non–melting snow as we will see later. Wind speed is assumed to become zero near the surface, depending on roughness length.

3.4.1 Background theory

The concept of atmospheric boundary layer (ABL) was introduced by Prandtl (1904) for the transport of momentum in the neighbourhood of a solid wall. It is assumed that the horizontal scales are much larger than the vertical and that the horizontal gradients and vertical velocities are negligible compared to the vertical gradients and horizontal velocities (Brutsaert 1982, p. 52). In the surface sublayer of the ABL, where turbulence is modulated or generated by wind shear near the ground, the vertical flux of horizontal momentum is:

$$\tau_{xz} = -\bar{\rho}\overline{w'u'}_s \quad and \quad \tau_{yz} = -\bar{\rho}\overline{w'v'}_s \tag{3.32}$$

where u, v, w are the Cartesian components of the wind vector, τ is stress and x, y, z the Cartesian axes, the overbar denotes mean values and prima denotes instantaneous values. The subscript s denotes values measured near the surface. The turbulent momentum flux acts like a stress (Stull 1988, p. 65), called the Reynold stress:

$$\tau_{Rey.} = \left[\tau_{xz}^2 + \tau_{yz}^2\right]^{1/2} \tag{3.33}$$

It is useful to introduce now a velocity scale, the friction velocity, which by definition is:

$$u_*^2 \quad = \quad \left[\overline{w'u'}_s^2 + \overline{w'v'}_s^2\right] \tag{3.34}$$

$$u_* \quad = \quad (\tau_{Rey.}/\rho)^{1/2} \tag{3.35}$$

The logarithmic wind profile law, also introduced by Prandtl (1932), and based on dimensional analysis, states that in a plan-parallel flow, wind mean speed increasing in the vertical direction ($d\bar{u}/dz$) indicates downward momentum flux and a sink at the surface. Measurements confirm that the profile is logarithmic in near–neutral atmospheres in the first few metres above the surface (Paterson 1994). Thus, in the dynamic sublayer, the fully turbulent region closer to the surface where Coriolis forces and buoyancy are negligible, we have:

$$\frac{u_*}{(z-d_0)(d\bar{u}/dz)} = k \tag{3.36}$$

integrating:

$$\bar{u} = \frac{u_*}{k} \ln\left(\frac{z-d_0}{z_0}\right) \tag{3.37}$$

where z_0, the roughness length, is an integration constant that can be interpreted as the height above surface where the wind speed becomes zero (typical values over snow and ice range from 0.001 mm to a few cm (Paterson 1994)); the term d_0 (Paeschke 1937) is the zero-plane displacement height, introduced for rough surfaces, where the zero level reference is at a certain height between the base and the top of the roughness elements; following Brutsaert (1982) it is computed as $(2/3.0)7.35z_0$; k is the von Karman's constant, an empirical constant the value of which is 0.40, although some other values have been suggested . A similar approach can be used for deriving expressions for specific humidity and

other scalar admixtures whose presence do not affect the dynamics of flow (Brutsaert 1982):

$$\frac{E}{u_*(z - d_0)\rho(d\bar{q}/dz)} = -a_v k \tag{3.38}$$

where a_v is the ratio of eddy diffusivity to eddy viscosity for water vapour and $\bar{q}$ is mean specific humidity. Similarly, for the flux of sensible heat H:

$$\frac{H}{u_*(z - d_0)\rho c_p(d\bar{\theta}/dz)} = -a_h k \tag{3.39}$$

where c_p is the specific heat of dry air at constant pressure ($= 1004.67\, JKg^{-1}K^{-1}$) and a_h is the ratio of eddy diffusivity to eddy viscosity for heat. Although some experiments suggest that $a_h = a_v > a_m$, a_m for momentum, Stull (1988, p. 204) finds no theoretical reason for this and suggest some pressure correlation contamination effect in the measurements. A value of 1.0 will be used here.

In the surface sublayer, the lower part of the ABL above the roughness obstacles, flow is relatively unaffected by roughness elements and Coriolis forces, but buoyancy due to density gradient must be considered. Following Brutsaert (1982) the vertical acceleration of an air parcel, can be approximated to:

$$: \ddot{z} = -\frac{g}{T_a}\left(\frac{\partial\theta}{\partial z} + 0.61 T_a \frac{\partial q}{\partial z}\right) \tag{3.40}$$

and the contribution of buoyancy to turbulent kinetic energy in a horizontally homogeneous surface sublayer is, to a close approximation:

$$\frac{g}{\rho T_a}\left[\left(\frac{H}{c_p}\right) + 0.61 T_a E\right] \tag{3.41}$$

Equations 3.40 and 3.41 describe the effect of atmospheric stability on turbulent transport. From the dimensionless analysis and equations 3.36, 3.38 and 3.39 the dimensionless characteristics of the turbulence depends on $z - d_0, \tau_0, \rho$ and buoyancy (Equation 3.41) (Brutsaert 1982). The combination of these four quantities into one dimensionless variable was proposed by Monin and Obukhov (1954) as:

$$\zeta = \frac{z - d_0}{L} \tag{3.42}$$

where the Obukhov's stability length L is defined as:

$$L = \frac{-u_*^3\rho}{kg\left[\left(\frac{H}{T_a C_p}\right) + 0.61\, E\right]} \tag{3.43}$$

where g is the acceleration of gravity(Obukhov 1946, Businger and Yaglom 1971).

Finally we get the profiles for wind speed, water vapour and heat, considering measurements at one

level and at the surface, as:

$$u_* = \frac{\bar{u}k}{\ln\left(\frac{z-d_0}{z_{0m}}\right) - \Psi(\zeta)} \tag{3.44}$$

$$E = \frac{(q_a - q_s)a_v \, k \, u_* \, \rho}{\ln\left(\frac{z_q-d_0}{z_{0v}}\right) - \Psi_{sv}(\zeta)} \tag{3.45}$$

$$H = \frac{(\theta_a - \theta_s)a_h \, k \, u_* \, \rho \, C_p}{\ln\left(\frac{z_t-d_0}{z_{0h}}\right) - \Psi_{sh}(\zeta)} \tag{3.46}$$

Subscripts m, v, h refer to momentum, water vapour and heat respectively. The air density ρ for a given pressure is computed as the sum of densities of dry air ρ_d and water vapour ρ_v (Brutsaert 1982, Jacobson 1999):

$$\rho_d = p_d/(R_d * T_a) \tag{3.47}$$

$$\rho_v = 0.622 * e_0/(R_d * T_a) \tag{3.48}$$

$$\rho = \rho_d + \rho_v \tag{3.49}$$

where the partial pressure of water vapour is $p_d = p_z - e_0$ and p_z is computed in Equation 3.11, R_d is the gas constant for dry air and $0.622 = 18.016/28.966$ is the ratio of the molecular weights of water and dry air. The specific humidity at screen level q_a and on the snow surface q_s is calculated as:

$$q = \rho_v/\rho \tag{3.50}$$

The Ψ_s functions are stability corrections, which depend on the Obukhov's stability length. There is some disagreement on their values, which have been obtained empirically (Brutsaert 1982, pp. 68-71). The values used here are similar to those used by Marks and Dozier (1992), also reported by Brutsaert (1982). Thus, for unstable conditions ($\zeta = (z_u - d_0)/L \leq 0$):

$$\Psi_{sv}(\zeta) = 2ln\left(\frac{1+\chi^2}{2}\right) \tag{3.51}$$

$$\Psi_{sm}(\zeta) = 2ln\left(\frac{1+\chi}{2}\right) + ln\left(\frac{1+\chi^2}{2}\right) - 2\arctan\chi + \frac{\pi}{2} \tag{3.52}$$

$$\Psi_{sh}(\zeta) = 2ln\left(\frac{1+\chi^2}{2}\right) \tag{3.53}$$

with $\chi = (1 - 16\zeta)^{1/4}$

For stable conditions ($\zeta = (z - d_0)/L > 0$):

$$\Psi_s(\zeta) = -\beta\zeta \quad \text{and} \quad \beta = 5 \tag{3.54}$$

A standard approach for the computation of the roughness length for momentum is to extrapolate the profiles of wind speed under neutral conditions to the level where wind speed equals zero (Stull 1988, Munro 1989, Greuell and Smeets 2001). However, this procedure requires measurements at at least two levels and is very sensitive to instrument errors. Furthermore, under katabatic winds the theoretical assumptions for estimating z_0 using the aerodynamical profile do not hold (Denby and Greuell 2000), therefore, a microtopographic survey is recommended. According to Brutsaert (1982), the value of z_0 is theoretically independent of the flow, except for flexible obstacles and waves), and only depends on the geometry of the surface. It was calculated as $z_0/h = 0.5\lambda$, where h is the roughness element height and λ is the frontal area index or vertical silhouette area per unit ground area (Lettau 1969). Data from wind tunnel experiments and atmospheric observations show that z_0/h increases linearly with λ for $\lambda < \lambda_{max}$ (Raupach 1992). The precise form of this function and the value of λ_{max} depends on the geometry of the roughness elements, but the above linear relationship was found satisfactory for very rough snow surfaces on Vatnajökull, Iceland, by Smeets et al. (1999). The frontal area index will change depending on wind direction, and so will the surface roughness length, sometimes on a very large range (Jackson and Carroll 1977). There is ample scope for inaccuracies using this method for variable roughness elements; however it is reassuring to notice that according to Denby and Greuell (2000), an order of magnitude error in the estimation of z_0 will only result in a 25% error in the turbulent fluxes estimation using the bulk method.

The transfer mechanisms of momentum and of other scalar admixtures are different at the surface, and consequently the roughness lengths have different values for momentum, water vapour and heat, which were calculated following Andreas (1987). He developed a fitting polynomial of the scalar roughness lengths over snow and sea ice (the coefficients for this are given in table 3.1):

$$\ln\left(z_s/z_0\right) = b_0 + b_1 \ln R_e + b_2(\ln R_e)^2 \tag{3.55}$$

where z_s refers to water vapour or heat depending on the coefficients used. The Reynolds number R_e is a ratio of inertial to viscous forces (Stull 1988) defined as:

$$R_e = \frac{u_*}{z_0\nu} \tag{3.56}$$

and $\nu = \mu/\rho$ is the kinematic viscosity of air, with μ the coefficient of dynamic viscosity for air.

	$R_e \leq 0.135$	$0.135 < R_e < 2.5$	$2.5 \leq R_e \leq 1000$
Temperature			
b_0	1.250	0.149	0.317
b_1	–	-0.550	-0.565
b_2	–	–	-0.183
Water vapour			
b_0	1.610	0.351	0.396
b_1	–	-0.628	-0.512
b_2	–	–	-0.180

Table 3.1. Values of the coefficients in the polynomials (equation: 3.55) that predict z_0/z for temperature and water vapour (Andreas 1987) for smooth, transition and rough surfaces.

3.5 Internal heat fluxes

Other energy inputs to the snow pack proceed from horizontal advection and conduction, heat due to ice deformation and in some cases geothermal heat. Except in the last case, which may be important, these fluxes are small compared to radiative and turbulent fluxes, and for simplicity they can be neglected (Greuell and Konzelmann 1994, Arnold et al. 1996).

3.6 Temperature fluctuation

From the previous formulation of long–wave radiative fluxes and for both latent and sensible turbulent fluxes it is clear that the temperature of the snow surface is a very relevant parameter. Measuring this temperature accurately and without perturbing the snow surface is a difficult task. Andreas (1986) proposed a new method for its measurement, but it requires additional instrumentation and may not be reliable under intense evaporation. When there is a mixture of snow and water under melting conditions, the whole surface is assumed to be at melting point, but at night and at high altitudes, where snow is dry, the estimation is more complicated. The sensors available for this study were thermistors, which have different emissivity than snow, and therefore are subject to a different rate of radiative cooling and heating (Brandt and Warren 1993). During the day, if they are exposed to direct solar radiation, their temperature raises considerably, melting surrounding snow and getting progressively buried. Thus, the recorded temperature may be approximate at night but unreliable during the day unless there is evidence of melting. The recorded temperature reflects the temperature of a thicker layer near the surface,and not the skin temperature. This layer is approximately equal to the largest dimension of the probe, as its position may change as it melts and gets buried. The actual value of snow surface temperature is only approximate.

To enable the modelling of the spatially distributed components of the energy balance for the whole

area of the glacier, which requires intense computation, a very simple approach was used to estimate snow surface temperature. The change in temperature of a given volume of snow is proportional to the energy input and to the thermal properties of the snow. For a one dimensional system atmosphere – snow surface layer – subsurface snow pack the thermodynamic equation describing the conservation of energy, neglecting melting and refreezing, can be described as (Koh and Jordan 1995, Greuell and Konzelmann 1994):

$$\rho_s c_s \frac{\partial T}{\partial t} = \frac{\partial}{\partial z}\left(k_s \frac{\partial T}{\partial z}\right) - \frac{\partial Q_s}{\partial z} \tag{3.57}$$

This equation is applied in a very simplified form following Oke (1987) and implemented using finite differences:

$$\frac{\Delta Q_s}{\Delta z} = C_s \frac{\Delta \bar{T}}{\Delta t} \tag{3.58}$$

where ΔQ_s is the flux density energy used to heat the snow at the surface, and C_s is the heat capacity of the snow $C_s = \rho_s c_s$, ρ_s is snow density and c_s is the specific heat of snow (2.09×10^3 J kg^{-1} K^{-1}). As the main energy input comes from the surface, while the subsurface remains at a relatively stable temperature, we need to consider the thermal conductivity of the snow and the energy losses to subsurface layers:

$$Q_g = -\kappa_{Hs} C_s \frac{\partial \bar{T}}{\partial z} \simeq -k_s \frac{\Delta \bar{T}}{\Delta z} \tag{3.59}$$

where κ_{Hs} is the thermal diffusivity of the snow and k_s its thermal conductivity.

The volume of snow considered is that affected by the daily temperature changes at the surface. This temperature oscillation decreases exponentially with depth, and its amplitude at any given distance from the surface can be estimated according to Oke (1987) by

$$\Delta \bar{T}_z = \Delta \bar{T}_0 e^{-z(\pi \kappa_{Hs} P)^{1/2}} \tag{3.60}$$

where P is the wave period. Brutsaert (1982, equation 6.43) has shown that, roughly, 95% of the wave is damped at a depth of $3(2\kappa_{Hs}/\omega)^{1/2}$, where $\omega = 2\pi/P$. For a daily oscillation in the conditions of the present study this equation yields a value of 0.31 m. This figure agrees well with snow temperature profiles measured on other high altitude Andean glaciers (Wagnon 1999, Figure 3.11).

If we look in detail at the components of the energy fluxes at the surface, we can separate them into two groups, one that affects the uppermost surface layer and the other that can penetrate to a certain depth. In the first group are the turbulent heat interchange, the thermal radiation and the near infrared component of the short–wave radiation. Following Greuell and Konzelmann (1994), 36% of the total short–wave radiation is classified in the band below 0.8μm, which is absorbed near the surface. The band above this wavelength penetrates the snow pack and in theory it should be attenuated following Beer's law. However, because the combined effect of absorption, scattering, and the rapid change of the spectral composition of the downward flux, the attenuation does not follow an exponential decay in approximately the first 40 cm (Warren 1982). The additional radiative cooling at the surface may result

in a temperature maximum located somewhere below the surface (Warren 1982, Brun et al. 1989, Koh and Jordan 1995), which in some cases may lead to subsurface melting. This case was detected by Koh and Jordan (1995) using a high frequency–modulated continuous radar wave, which, by detecting changes in the dielectric properties of the snow, can determine accurately the onset of melting in internal layers. In the high Andes it was observed that the uppermost layer about 2.5 cm thick, was almost permanently frozen, while snow underneath was loose, with grains unbounded. This was likely to be caused by radiative cooling and negative turbulent heat transfer at the surface, while shortwave radiation penetrates underneath the surface. In order to replicate this situation in a simplified model, the snow pack was divided in two layers, the first one about 2.5 cm depth from the surface and a second sub-surface layer from -2.5cm to the depth where the daily temperature wave is almost damped (31 cm, 3.6). The energy fluxes and temperature variations modelled for both layers.

3.7   Model validation and applicability

To gain some confidence in the performance of the model and its application to a wide range of conditions, it was compared to data collected both in the Andes and at the Haut Glacier d'Arolla.

3.7.1   Short–wave validation

Figure 3.4 shows the recorded and measured short–wave radiation. Modelled radiation is separated into direct, diffuse and diffuse–reflected components. At this stage the modelled values do not incorporate cast shadows but take into account the slope of the ground. The AWS was situated on a gently sloping section of the glacier (10°to the west). The modelled values derive this inclination from the gradient of the corresponding cell in the digital elevation model. Neglecting this slope results in a large error and a different distribution of incoming solar radiation during the day. Figure 3.5 shows the values of measured and modelled solar radiation for Loma Larga glacier, at 4667 m a.s.l. Errors in both cases are smaller than the pyranometer accuracy.

3.7.2   Long–wave validation

In the Andes direct measurements of long–wave radiation were not available, thus only data from Arolla is used here for the validation. Net long–wave radiation was estimated from the difference between measured net all–wave radiation and measured net short–wave radiation. Net all–wave radiation was measured with a Kipp & Zonen NR–Lite net radiometer and net short–wave radiation is derived from the values measured by two Kipp & Zonnen opposed pyranometers. The NR-Lite net radiometer is a simple, low maintenance instrument, and even when daily values are within the nominal accuracy, the
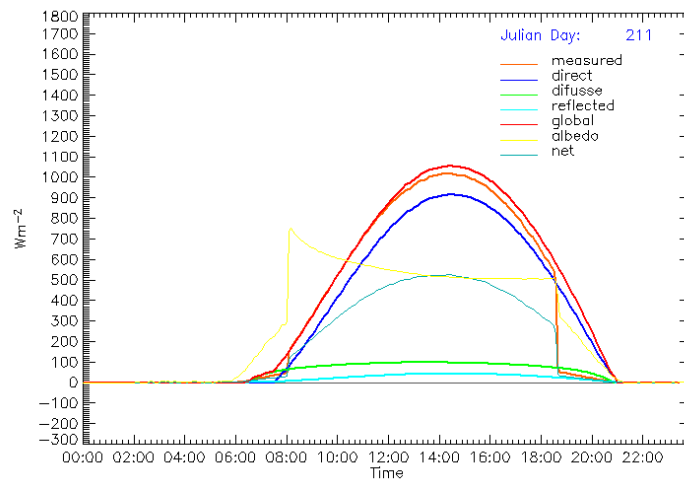
Figure 3.4. Measured and modelled short–wave radiation at the Haut Glacier d'Arolla, 2900m a.s.l., Swiss Alps, on a typical clear day. Diffuse radiation is separated into that from sky and that from surrounding slopes. The fit is better than the accuracy of the pyranometer (10%). 7 LINES ONLY 6 LEGEND
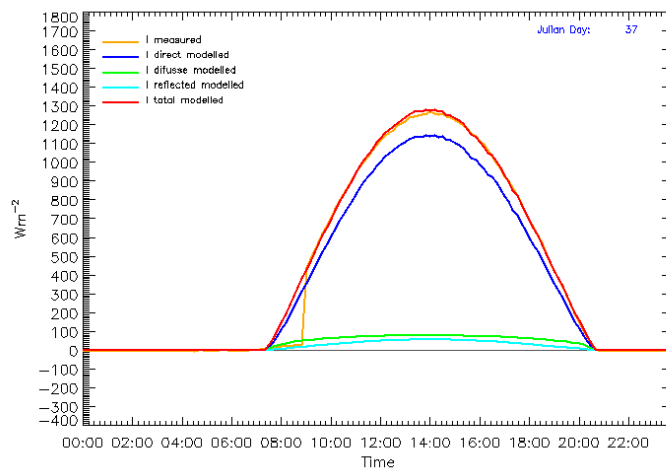

Figure 3.5. Measured and modelled short–wave radiation at Loma Larga glacier, 4667 m a.s.l. Diffuse radiation is separated into that from sky and that from surrounding slopes. For the aerosol transmittance, visibility is assumed to be 100 km through the whole day, whereas for other transmittances, meteorological variables recorded at 10 minute interval were used. The fit is better than the accuracy of the pyranometer (10%). Cast shadows and the fraction of shaded surrounding slopes are not computed at this stage.

different responses of the two instruments produces some artifacts in the data, as the pronounced troughs in Figure 3.6 near sunset and sunrise. After consultation with Campbell Scientific UK, it was concluded that these troughs are likely to be caused by the different cosine response of the net radiometer and the

pyranometers, plus some delay in the time response of the net radiometer.
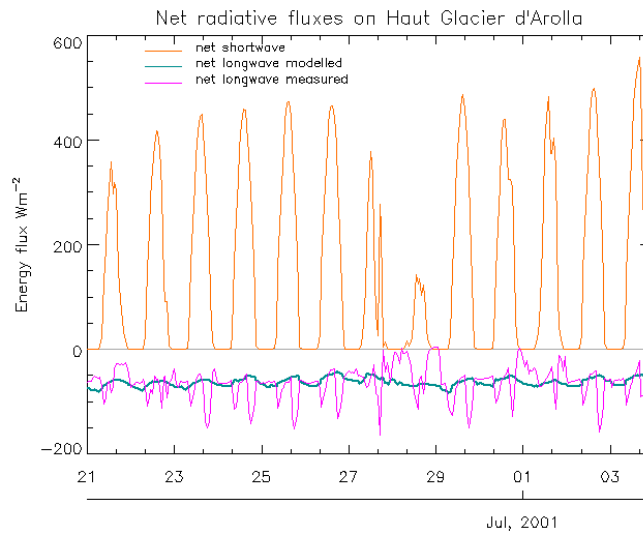

Figure 3.6. Modelled and measured net long–wave radiation for a 2–week period in summer 2001 at the Haut Glacier d'Arolla, Swiss Alps. Note that the pronounced troughs in measured long–wave are likely to be instrumental artifacts, as explained in the text, and that values are modelled only for clear skies, so peaks under cloudy conditions are not reproduced. The average difference between modelled and measured values under cloudless skies, after discharging near sunset and near sunrise values, is less than 1%.

3.7.3 Snow temperature model validation

The modelling of surface temperature requires a detailed knowledge of the energy balance, but the computation of the energy balance requires a detailed knowledge of the surface temperature. It would be a difficult problem to solve if it were not for the fact that the whole process is strongly stable and there are a number of feedbacks involved which tend to make all the related variables in the model converge to realistic values. Thus, if there are clear boundary conditions, the whole process of energy balance and snow surface temperature can be modelled within a narrow margin. The stability of the process is illustrated in figures 3.7 and 3.8, where the initial temperature was set to 200 K. Fluxes at any time step i are modelled with the temperature calculated at time step $i-1$ and then T_i recalculated with the computed fluxes. Establishing an arbitrary low T_0 allows the testing of the convergence of the model to real values and also its stability. The convergence speed of modelled and measured values is inversely related to the thickness of the uppermost snow layer, but in any case it only takes a few timesteps.

Figure 3.7 shows the measured and modelled temperatures of the total surface layer for a two week period on Loma Larga glacier, 4667m a.s.l. The glacier was covered in penitentes, and the two measured temperatures were at different positions on the surface of penitentes (T_1 near the penitentes' trough and
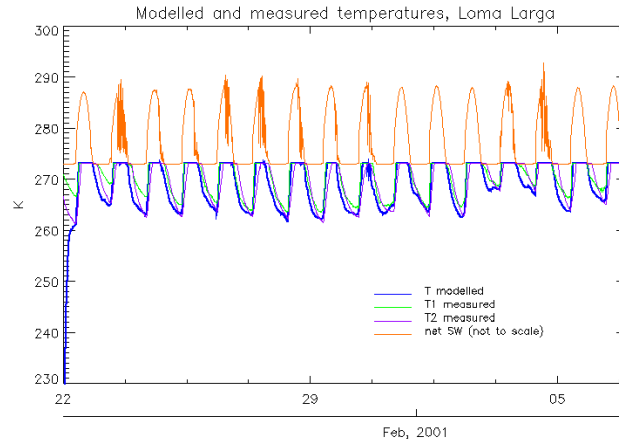
Figure 3.7. Comparison between modelled and measured temperatures on the surface of Loma Larga glacier, 4667 m.a.s.l. The surface was covered in snow penitentes and the measurement sites at T1 (closer to the bottom of penitentes) and T2 (closer to the penitentes' peak) had a slightly different net energy flux. Site T2 was likely to undergo a more intense radiative cooling. Initial modelled temperature was set to -73.15°C (200 K) to assess the stability of the model and the rapid convergence of modelled values to measured ones.
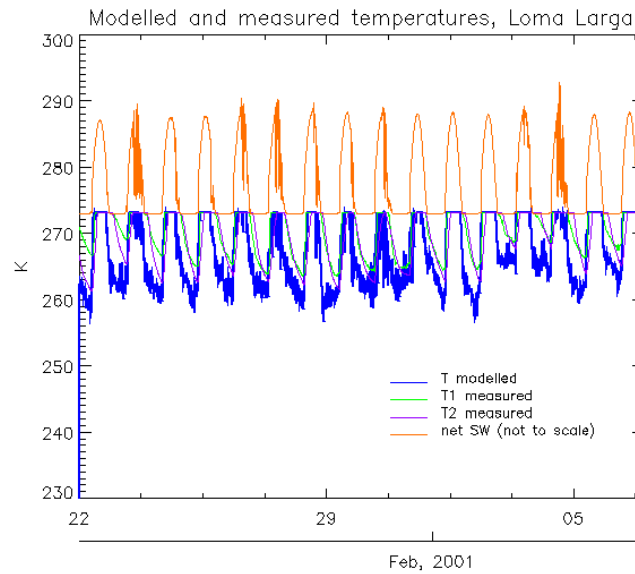
Figure 3.8. Comparison between modelled and measured temperatures on the surface of Loma Larga glacier, as in Figure 3.7, but modelled for the uppermost surface layer, about 2 cm depth.

T_2 closer to the peaks). This resulted in different sky view configurations and differences in the incoming and outgoing long–wave radiative fluxes, and therefore different rates of radiative cooling. Additional delays in the lowering of recorded temperature, especially when direct solar radiation decreases, may be

due to the presence of liquid water in the troughs between penitentes. Water has higher specific heat and therefore is likely to have a buffering effect in the temperature fluctuations. The modelled temperature is for an intermediate value of sky view factor and for the whole surface layer. Figure 3.8 shows modelled temperature for the uppermost surface layer, about 2.5 cm in depth. Here variation is faster and minimum temperatures are attained very soon. According to values of skin temperature measured with a hand held infrared thermometer, this second situation is likely to be more realistic. Values show a very rapid change within a range of a few degrees, normally associated with wind gusts, suggesting the importance of latent heat fluxes in the cooling of the surface. For the global evaluation of the energy balance, both surface and subsurface layers were considered, as indicated in Figure 3.7. However, the detailed variation of the thin, uppermost surface layer may be of interest to the initial process of snow metamorphism and micropenitentes formation. It would be desirable a precise recording of its temperature fluctuations in order to minimise errors derived from model simplifications. There are no snow surface temperature measurements for Arolla.

3.7.4   Net energy balance and melt validation

To asses all the modelled fluxes at the snow surface, the net energy balance is estimated and the corresponding melt computed. Figure 3.9 shows the measured and modelled fluxes at the AWS on Loma Larga glacier. An unusual pattern is observed in the last hours of the afternoon, when the albedo values rise sharply to almost 1.0. It may be the effect of a nearby icefall, which increases the diffuse radiation, or it could be explained by a sharp increase in reflected diffuse radiation as the sun hits the penitentes' slanting wall from the west at a very low angle. Snow is not a perfect lambertian reflector, the reflected diffuse radiation field having a prominent forward lobe at low incident angles (Warren 1982), thus at high zenith angles the upward component of the reflected radiation may increase considerably, especially when the sun hits the sloping back walls of the penitentes. The fact that the increase in albedo happens after 1800 h (Figure 3.10, when the solar azimuth enters the southwestern quadrant, adds support to this hypothesis.

There were no independent measurement of sensible and latent fluxes available for the present work, nor evaporation measurements; therefore it is impossible to make a strict and rigorous assessment of the accuracy of the method. However, it has been used successfully on snow research in previous cases, over a wide range of climatic conditions (Marks and Dozier 1992, Plüss and Mazzoni 1994, Arnold et al. 1996, Aizen et al. 1997, Brock and Arnold 2000, Obleitner 2000), and it seems appropriate for sites where evaporation is an important component of the energy balance (Marks and Dozier 1992, Aizen et al. 1997). Figure 3.11 shows the application of the whole energy balance to estimating melt at a point during a 2–week period in summer 2001 on the Haut Glacier d'Arolla. Ablation was measured with a Campbell SR50 ultrasonic snow depth gauge and compared to modelled ablation. Precipitation is included, but estimating the right amount of precipitation is problematic. Firstly rain gauges are not very accurate when rain or snow falls during windy conditions. Secondly the rain gauge was at the snout
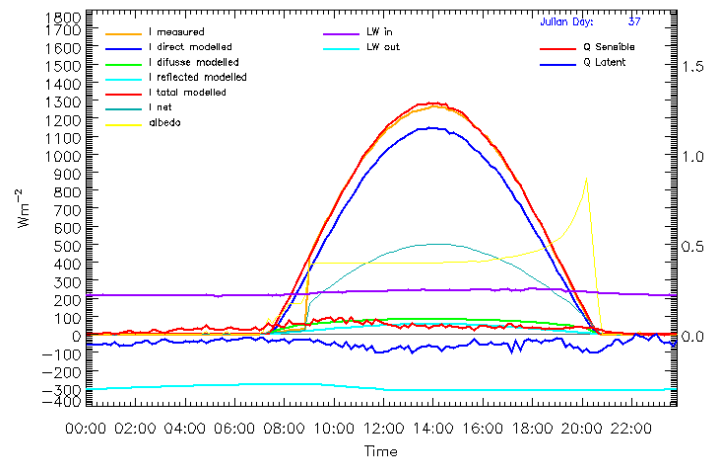
Figure 3.9. Energy fluxes on a clear day on Loma Larga glacier, 4667 m a.s.l. DOY 37, 6th of February. Note the increasing albedo in the afternoon, when the apparent position of the sun changes from north to south (see Figure 3.10), an explanatory hypothesis is given in the text.
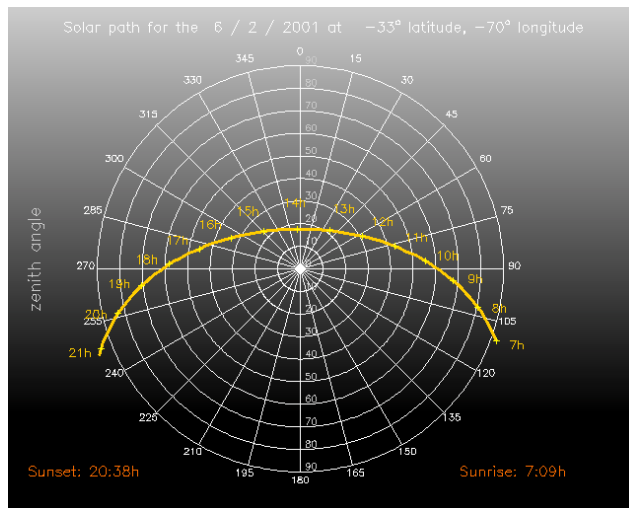

Figure 3.10. Solar path for the day 37 (6 February, 2001) at $33°\,$S, $10°\,$W. The sun crosses to the southern apparent position at about 18:00, when the recorded albedo starts to increase (see text for tentative explanation). I have made the IDL code for plotting the solar path available at the IDL user contributed library at www.rsinc.com/ .

of the glacier, a few kilometres away from the ultrasonic gauge. Finally, the conversion of new snow to depth equivalent depends on snow density and wind redistribution, which are difficult to evaluate. From Figure 3.11 it seems that the pattern of modelled and measured melting follows a close relationship until day 29, a cloudy day, with little energy available for melting. Here the model underestimates total melting, and the cause could be an underestimation of turbulent fluxes or an anomalous high value of radiative cooling, as can be deduced from the very low trough in net radiation. This trough is also rather anomalous, one would expect a minimum value on very clear nights, and it could be hypothesized that such a situation is likely to happen after the pass of a perturbation and the clearing up of clouds in a

cleaner air. However a more sophisticated Kipp & Zonen CNR1 net radiometer in the lower section of the valley did not record this trough, which suggests an instrumental artifact. It is worth saying that Plüss and Mazzoni (1994) noted the underestimation of total melt energy using a bulk method when compared to total melt directly measured with a lysimeter, and Hock (2002) noted that calculated melt energy was underestimated in days with precipitation or dense fog in her study of Storglaciaren, in northern Sweden. These discrepancies recommend a more detailed survey of modelled and measured melt values, even when as in the examples given here, modelled results agree within a few percent of measured ones.

A comparison of calculated melt with sparse data from ablation stakes in Juncal Norte glacier near the lower AWS in the Andes campaign is shown in Figure 3.12, where the symbols show measured values from ablation stakes and the stepping line is modelled melt. The main uncertainties derive from the exact estimation of the snow density and surface temperature and from errors inherent in the stake ablation method, such as snow compactation, stake deepening, etc. Nonetheless, the difference between modelled and measured values over a 11–day period is less than 2 cm or 3.3%.
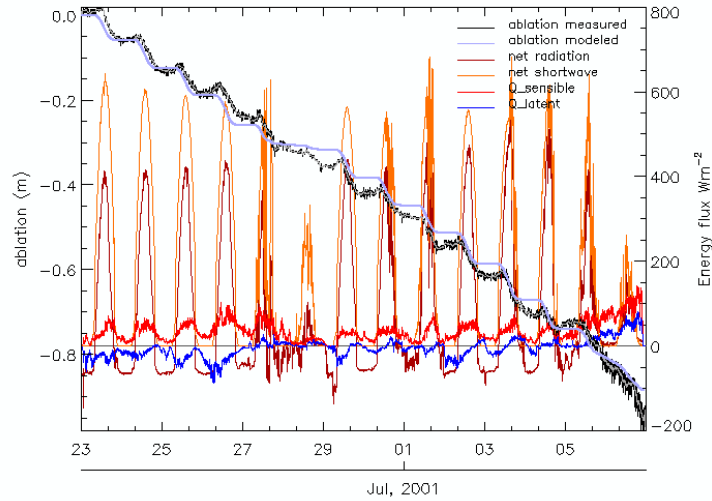
Figure 3.11. Energy balance components, modelled melt and measured snow depth at the Haut Glacier d'Arolla for a 2 week period in July 2001.
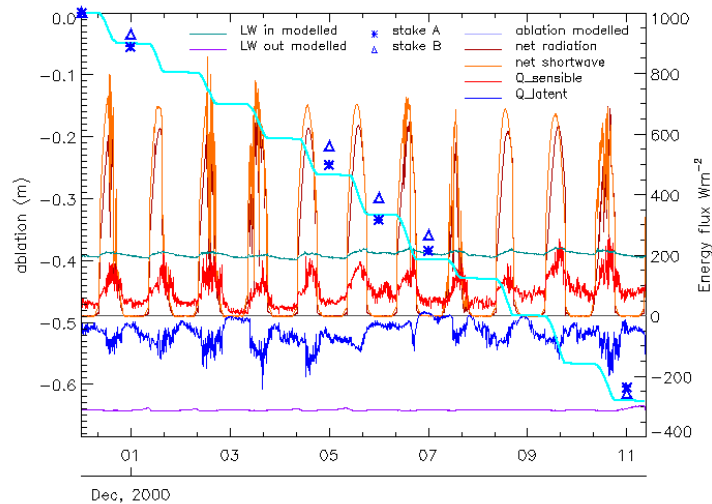

Figure 3.12. Energy balance components, modelled melt and measured snow lowering from ablation stakes on Juncal Norte glacier, 3035 m a.s.l. for a 11–day period in November–December, 2000. Note the maximum values of turbulent heat fluxes that correspond to wind speeds higher than $10ms^{-1}$ and relative humidity lower than 20%.